

PAPER • OPEN ACCESS

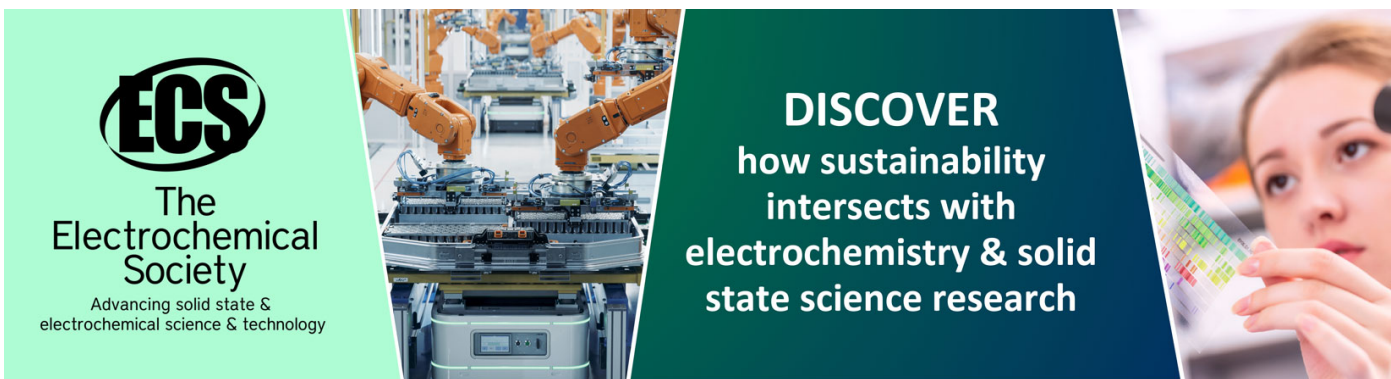
Image processing: Obtaining more information from satellite aerosol imagery over West Africa

To cite this article: M.E. Emetere *et al* 2019 *J. Phys.: Conf. Ser.* **1299** 012043

View the [article online](#) for updates and enhancements.

You may also like

- [Air pollution Estimation Over Bouake](#)
M.E. Emetere and M.O. Ahiara
- [Wavelet-based 2D fusing of ultrasonic pulse-echo traces measured from two arrays radiating orthogonal beams](#)
Miguel A Rodríguez-Hernandez, Antonio Ramos and J L San Emeterio
- [Air pollution Indexes Over Buchanan: Danger and Control](#)
M.E. Emetere, Okoro Emeka Emmanuel, Sanni E. Samuel et al.



ECS
The
Electrochemical
Society
Advancing solid state &
electrochemical science & technology

DISCOVER
how sustainability
intersects with
electrochemistry & solid
state science research

Image processing: Obtaining more information from satellite aerosol imagery over West Africa

Emetere M.E.^{1,2}, Emetere J.M.³ and Akinyemi M.L.¹

¹Department of Physics, Covenant University, Ota, Nigeria.

²Department of Mechanical Engineering & Science, Univ. of Johannesburg, APK, South Africa

³Federal University of Technology Minna, Nigeria

emetere@yahoo.com

Abstract. The conventional way for interpreting satellite imagery is the color codes that appear on the color bar. Recent trends of image-processing show the complexity of camera technology. The satellite imagery used for this research is obtained from the Multi-angle Imaging SpectroRadiometer (MISR). The image processing was done using CERN-Root open source and C++ language. The results show that vital information can be obtained via image processing techniques.

1. Introduction

Aerosols distribution over West Africa region is unique because of the volume of anthropogenic aerosol dispersion over the region [1]. The mathematics of aerosol dispersion has been propounded [2] and has been verified in over sixty locations within major cities or towns in West Africa [3-8]. Researchers have used satellite imagery to discuss aerosols distribution in parts or sectional portions of West Africa [9-10]. Image processing of satellite images according to literature relates to either atmospheric correction of satellite images [11] or satellite image processing algorithm [12].

This article focuses on the need to focus on the re-processing of satellite imagery using open source software to decipher additional information.

2. Methodology

The satellite imagery for West Africa regional was obtained from the NASA-MISR for the year 2013. The raw satellite image is shown in Figure 1. The satellite image is a MOD08_D3.051 aerosol optical depth pixel count. The properties of the images were obtained using the MAC inbuilt-library for determining image properties. The satellite image was harvested in .gif format. The first method is to convert the satellite image from .gif to .png file. The properties of the new image are verified using the afore-mentioned technique.

The CERN Root open software was used to determine parameters like, 2D imagery, spectrum imagery, intensity of image, standard deviation of individual pixels in the image, full width at half maximum (FWHM), Mean pixel, X and Y projections. The opencv C++ library were used to obtain the various contours that were not visible to the human eye.



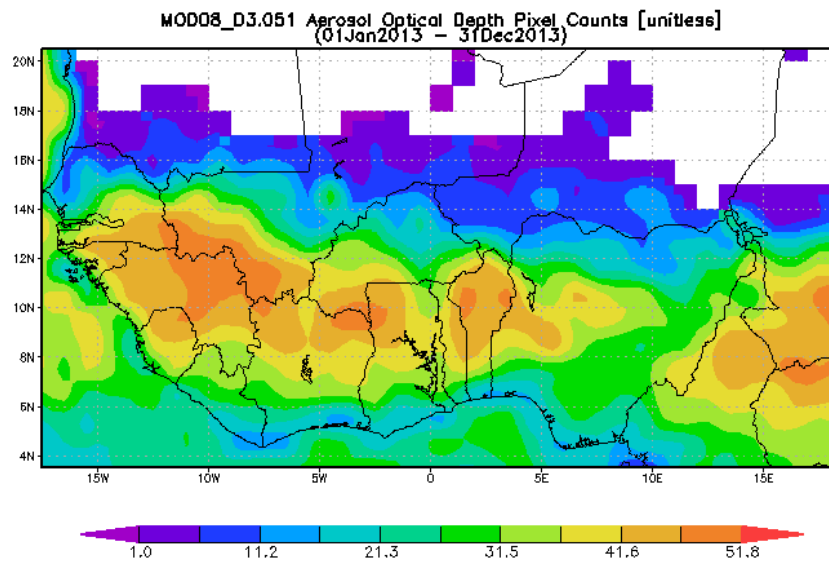


Figure 1: Satellite imagery for West Africa, 2013

In order to understand the dynamics of the atmospheric convection of the dispersion, equation (1) is resolved in accordance to the Lorentz atmospheric convection model.

$$\frac{\partial C}{\partial t} + V_x \frac{\partial C}{\partial x} - V_z \frac{\partial C}{\partial z} - V_y \frac{\partial C}{\partial y} = \frac{\partial}{\partial z} \left(K_z \frac{\partial C}{\partial z} \right) + \frac{\partial}{\partial y} \left(K_y \frac{\partial C}{\partial y} \right) + \frac{\partial}{\partial x} \left(K_x \frac{\partial C}{\partial x} \right) + \frac{\partial}{\partial y} \left(K_{y2} \frac{\partial C}{\partial y} \right) - P + S \tag{1}$$

$$\text{let } \frac{\partial t}{\partial z} \approx \frac{1}{z}, \frac{\partial t}{\partial y} \approx \frac{1}{y}, \frac{\partial t}{\partial x} \approx \frac{1}{x} \text{ and } \frac{\partial C}{\partial t} \approx C_t$$

$$\left. \begin{aligned} \frac{\partial C}{\partial z} &= \frac{\partial t}{\partial z} \times \frac{\partial C}{\partial t} \\ \frac{\partial C}{\partial x} &= \frac{\partial t}{\partial x} \times \frac{\partial C}{\partial t} \\ \frac{\partial C}{\partial y} &= \frac{\partial t}{\partial y} \times \frac{\partial C}{\partial t} \end{aligned} \right\} \tag{2}$$

Hence $\frac{\partial C}{\partial z} = \frac{C_t}{z}, \frac{\partial C}{\partial y} = \frac{C_t}{y}, \frac{\partial C}{\partial x} = \frac{C_t}{x}$

Let $\frac{\partial}{\partial y} \left(K_{y2} \frac{\partial C}{\partial y} \right) = 0, \frac{\partial}{\partial z} \left(K_z \frac{\partial C}{\partial z} \right) = 0, \frac{\partial}{\partial y} \left(K_y \frac{\partial C}{\partial y} \right) = 0, \frac{\partial}{\partial z} \left(K_{z2} \frac{\partial C}{\partial z} \right) = 0$

Hence, equation (1) becomes

$$\frac{\partial C}{\partial y} = \frac{C_t}{V_y} + \frac{V_x C_t}{V_y x} - \frac{V_z C_t}{V_y z} + \frac{P}{V_y} - \frac{S}{V_y} \tag{3}$$

since

$$\frac{\partial t}{\partial y} = \frac{1}{V_y} + \frac{V_x}{V_y x} - \frac{V_z}{V_y z} + \frac{P}{C_t V_y} - \frac{S}{C_t V_y}$$

$$\frac{\partial y}{\partial t} = V_y + \frac{V_{yx}}{V_x} - \frac{V_{yz}}{V_z} + \frac{C_t V_y}{P} - \frac{C_t V_y}{S} \quad (4)$$

$$\text{Let } \alpha = \frac{V_y}{V_x}, \beta = \frac{V_y}{V_z}, \rho = \frac{V_z}{V_x}$$

The inverse of equation (4) becomes

$$\frac{\partial y}{\partial t} = \alpha x - \beta z + V_y + \frac{C_t V_y}{P} - \frac{C_t V_y}{S} \quad (5)$$

Using the same principle,

$$\frac{\partial z}{\partial t} = \rho x - \frac{y}{\beta} + V_z + \frac{C_t V_z}{P} - \frac{C_t V_z}{S} \quad (6)$$

$$\frac{\partial x}{\partial t} = \frac{z}{\rho} + \frac{y}{\alpha} - V_x - \frac{C_t V_x}{P} + \frac{C_t V_x}{S} \quad (7)$$

Results and Discussion

The picture properties of the raw satellite information and the changed over information is appeared Table 1. It is seen that the new pictures enhanced the dpi (Dots Per Inch) width, dpi height, test per pixel, pixel width and pixel height.

Table 1: Image properties

Number	Parameters	Old Image	New Image
1	pixelWidth	700	1242
2	pixelHeight	500	646
3	typeIdentifier	com.compuserve.gif	public.png
4	format	gif	png
5	dpiWidth	72.000	144.000
6	dpiHeight	72.000	144.000
7	samplesPerPixel	3	4
8	bitsPerSample	8	8
9	hasAlpha	no	yes
10	space	RGB	RGB
11	profile	sRGB IEC61966-2.1	Color LCD

The pixel along the X and Y axes were plotted as shown in Figure 2. A comparative view of Figures 1 & 2 show region that is invisible to the human eye (see red arrows).

The contour location calculation was utilized to decide shapes not noticeable to the eye. The circles are utilized to gauge the width of the shape for example since the width of the circle. The blue bolt demonstrates the immaterial circle in light of the fact that the form inside the circle is a territorial limit. The red bolt demonstrates the significant circle that contains forms that can't be spotted by the human eye (Figure 3). 40% of the circles really indicate the valuable forms while about 60% just identifies with limit lines. The sizes of the circle can be estimated and the given areas inside the circle can be explored for more data. The 3D picture (Figure 4) demonstrates the connection between the inferred grids of the picture.

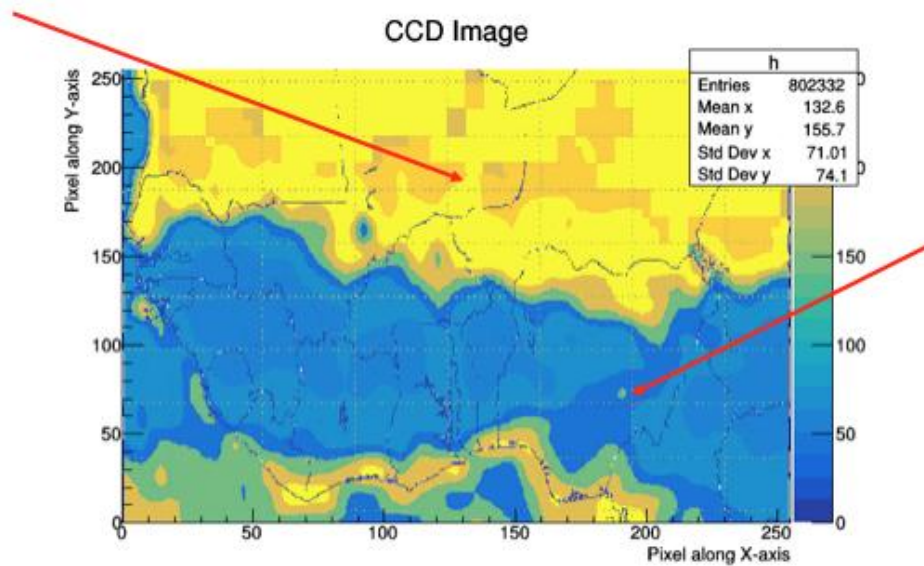


Figure 2: Matrix plot of X and Y dimension



Figure3: Contour detection of satellite image

The red arrow corresponds to locations under intense influence of the Sahara dust (Figure 4). The purple arrow shows locations on Figure 1 that have mechanisms of dousing the influence of Sahara dust via wind convection or rainfall patterns [3-4]. Figures 5 and 6 show the X and Y projections of Figure 1. The X-projection relates the X-segment of the satellite picture in extent of pixels along the x-pivot of Figure 1. For instance, on the pixel 150 and 200, the X-segment of the absolute pixels is most elevated over Nigeria, Chad and so forth. Likewise, two (165 and 190) was most extreme which obviously demonstrates that there is higher mist concentrates scattering along these focuses. Additionally, considering the Y-Projection of Figure 1 for example the greatness of pixels along the y-hub, it very well may be seen that the pixel achieves its most extreme qualities over 170. This further certifies the overwhelming impact of the Sahara along the upper pieces of Figure 1.

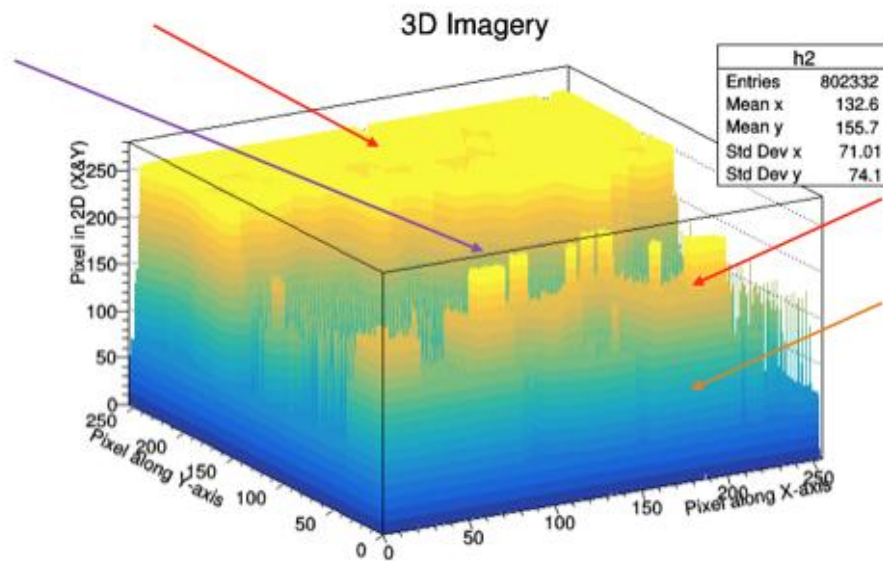


Figure 4: 3D setting of satellite image

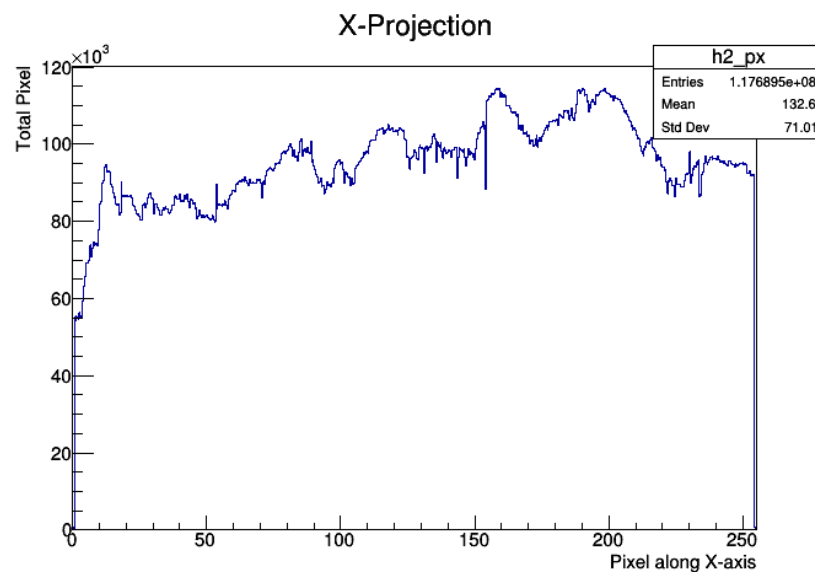


Figure 5: X-projection of satellite image

The spectrum analysis of the satellite image (Figure 1) is shown in Figure 7. The spectrum analysis shows the vertical profile and turbulence of aerosols. The aerosols activities i.e. dispersion, distribution and loading are illustrated by the colour-mix represented. For example, the red arrow shows the influence of Sahara on the given locations. The vertical profiles (green arrow) show that aerosols forms layers within the atmosphere. The purple arrow shows the distribution of other anthropogenic pollution source.

To understand the parametric dynamics of aerosol loading over Nouakchott, the Lorentz form expressed in equations (5-7) will be used because it is notable for having chaotic solutions for certain parameter values and initial conditions. The particulate velocities were considered in three coordinates i.e. x, y and z. The initial conditions are given as 1 m/s for each coordinates. Three cases were

considered i.e. plume condition during ascension, uniform motion and deposition. Table 2 show the plume ascension condition. It is observed that the velocities of the particulates decrease within travel time. However, the particulate velocity in the x-direction diminishes faster than the other velocities at about 1.8 times. When the plume is in a uniform motion, the particulate velocity in the x-direction diminishes faster than the other velocities at about 1.6 times. The particulate velocities in the y and z directions were noticed to be almost the same during aerosol loading at uniform motion. During deposition (Table 4), the particulates in the y-direction decrease exponentially into the negative. This behaviour rightly describes the unpredictability of atmospheric aerosols deposition in large-scale events.

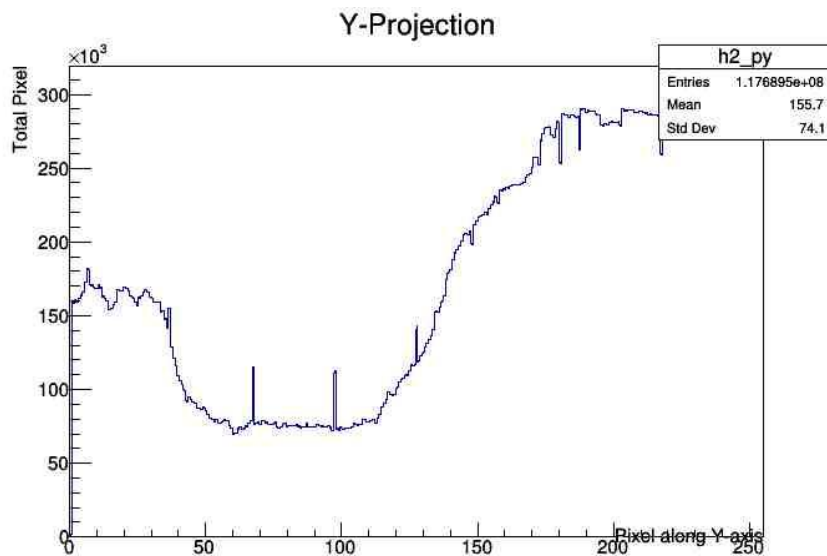


Figure 6: Y-projection of satellite image

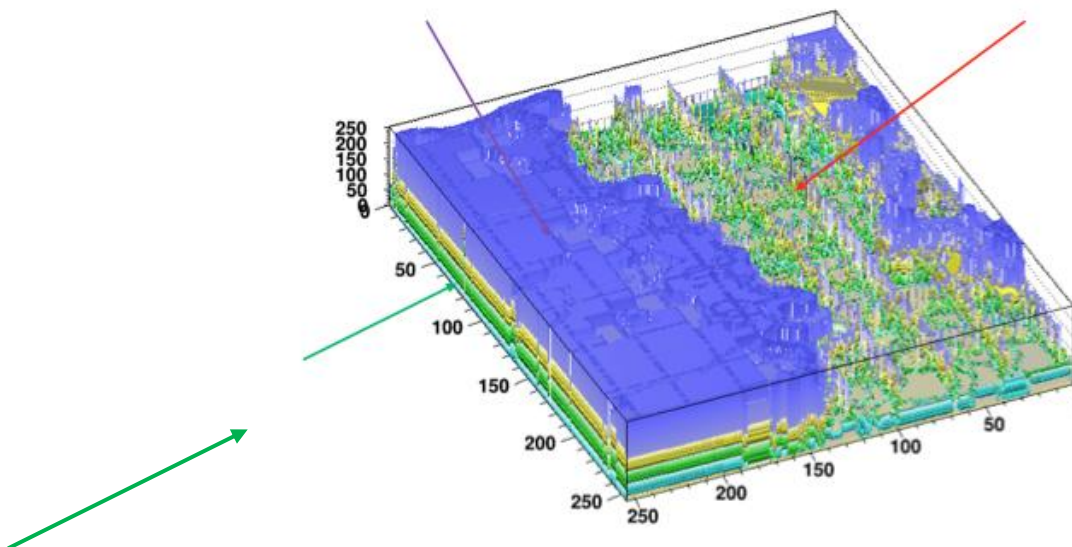


Figure 7: The spectrum analysis of the satellite image

Table 2: Dynamics of particulate velocities along specific coordinates during plume ascension

When particulates move-up $V_x=0.8, V_y=0.8, V_z=1.5, P=10, S=8/3$			
t(s)	Dx/Dt	Dy/Dt	Dz/Dt
0	1	1	1
0.1	0.607954	1.0294	1.17037
0.213228	0.421761	0.978745	1.20083
0.326457	0.321511	0.86811	1.05589
0.44633	0.254731	0.729429	0.831077
0.575517	0.205643	0.589425	0.615282
0.716873	0.167138	0.463323	0.443491
0.87404	0.135513	0.356561	0.316299
1.05231	0.108627	0.268906	0.223891
1.26136	0.0850238	0.197408	0.156027
1.4854	0.0661078	0.145029	0.110329
1.71975	0.0512069	0.107198	0.0793292
1.9541	0.0398788	0.0805066	0.0584295
2.19989	0.0308041	0.0603951	0.0431974
2.44568	0.0238655	0.045759	0.032384
2.69147	0.0185304	0.0349288	0.024527
2.93727	0.0144117	0.0268122	0.018718
3.18306	0.0112226	0.0206698	0.0143665
3.42885	0.00874759	0.0159867	0.0110743
3.67464	0.0068235	0.0123956	0.00856469
3.92043	0.00532569	0.00962968	0.0066405
4.16623	0.00415852	0.0074921	0.00515861
4.41202	0.00324828	0.00583574	0.00401341
4.65781	0.00253797	0.00454964	0.00312607
4.9036	0.00198341	0.00354945	0.0024371
5.14939	0.00155027	0.00277063	0.00190131
5.39518	0.00121189	0.00216362	0.00148411
5.64098	0.000947455	0.00169015	0.00115895
5.88677	0.000740781	0.00132063	0.000905331
6.13256	0.000579225	0.00103211	0.000707395
6.37835	0.000452925	0.000806742	0.000552845
6.62414	0.000354178	0.000630665	0.000432129
6.86993	0.000276968	0.000493065	0.000337813
7.11573	0.000216595	0.000385516	0.000264108
7.36152	0.000169385	0.000301443	0.000206499

7.60731	0.000132466	0.000235715	0.000161466
7.8531	0.000103596	0.000184326	0.000126259
8.09889	8.10183e-05	0.000144144	9.87329e-05
8.34469	6.33617e-05	0.000112724	7.72098e-05
8.59048	4.95533e-05	8.81545e-05	6.03798e-05
8.83627	3.87543e-05	6.8941e-05	4.72193e-05
9.08206	3.03088e-05	5.39157e-05	3.69277e-05
9.32785	2.37039e-05	4.21654e-05	2.88795e-05
9.57364	1.85383e-05	3.29762e-05	2.25856e-05
9.81944	1.44984e-05	2.57897e-05	1.76634e-05
10	1.21032e-05	2.1529e-05	1.47452e-05

Table 3: Dynamics of particulate velocities along specific coordinates during plume uniform motion

When particulates uniformly $V_x=0.8, V_y=0.8, V_z=0.8, P=10, S=8/3$			
t(s)	Dx/Dt	Dy/Dt	Dz/Dt
0	1	1	1
0.1	0.676254	1.09086	1.09086
0.231059	0.47831	1.12783	1.12783
0.362117	0.369642	1.06904	1.06904
0.502941	0.2949	0.937669	0.937669
0.653936	0.239252	0.774504	0.774504
0.818304	0.194903	0.612804	0.612804
1.00037	0.157832	0.469781	0.469781
1.20741	0.125656	0.349869	0.349869
1.42809	0.0993402	0.259367	0.259367
1.66051	0.0779591	0.192385	0.192385
1.90165	0.0608256	0.143268	0.143268
2.14278	0.0475552	0.108008	0.108008
2.39232	0.0369137	0.0814334	0.0814334
2.64187	0.0286812	0.0618733	0.0618733
2.89141	0.0222999	0.0472877	0.0472877
3.14096	0.017347	0.0363019	0.0363019
3.3905	0.0134992	0.0279632	0.0279632
3.64005	0.0105078	0.021596	0.021596
3.88959	0.00818111	0.016712	0.016712
4.13914	0.00637066	0.0129525	0.0129525
4.38868	0.0049615	0.0100506	0.0100506
4.63823	0.00386442	0.00780605	0.00780605

4.88777	0.00301016	0.00606707	0.00606707
5.13732	0.00234488	0.00471809	0.00471809
5.38686	0.00182673	0.00367062	0.00367062
5.6364	0.00142312	0.00285665	0.00285665
5.88595	0.00110872	0.00222375	0.00222375
6.13549	0.000863797	0.00173142	0.00173142
6.38504	0.000672991	0.0013483	0.0013483
6.63458	0.000524339	0.00105009	0.00105009
6.88413	0.000408527	0.000817909	0.000817909
7.13367	0.000318297	0.000637112	0.000637112
7.38322	0.000247997	0.000496309	0.000496309
7.63276	0.000193225	0.000386641	0.000386641
7.88231	0.00015055	0.000301216	0.000301216
8.13185	0.000117301	0.000234672	0.000234672
8.3814	9.13946e-05	0.000182832	0.000182832
8.63094	7.12102e-05	0.000142446	0.000142446
8.88049	5.54835e-05	0.000110983	0.000110983
9.13003	4.32301e-05	8.64697e-05	8.64697e-05
9.37958	3.36829e-05	6.73715e-05	6.73715e-05
9.62912	2.62441e-05	5.24917e-05	5.24917e-05
9.87867	2.04482e-05	4.08985e-05	4.08985e-05
10	1.81118e-05	3.62252e-05	3.62252e-05

Table 4: Dynamics of particulate velocities along specific coordinates during plume deposition

When particulates uniformly $V_x=0.8, V_y=0.8, V_z=0.2, P=10, S=8/3$			
t(s)	Dx/Dt	Dy/Dt	Dz/Dt
0	1	1	1
0.1	0.631079	1.60889	1.01599
0.221816	0.444675	4.20314	1.00428
0.343633	0.346784	-12.512	0.963795
0.465449	0.284886	-2.87007	0.902982
0.587266	0.241142	-1.72187	0.830492
0.721537	0.204895	-1.23813	0.745557
0.865749	0.174566	-0.970896	0.655697
1.02075	0.148441	-0.795453	0.565875
1.18742	0.125516	-0.666194	0.47992
1.36678	0.105199	-0.562662	0.400365

1.55994	0.0871609	-0.474765	0.328696
1.76774	0.0712423	-0.39751	0.265653
1.9904	0.0573857	-0.32875	0.21149
2.22684	0.0455747	-0.267966	0.166115
2.47442	0.035768	-0.215367	0.12911
2.72201	0.028044	-0.172267	0.100433
2.9696	0.0219692	-0.137183	0.0781818
3.21719	0.017198	-0.108826	0.0608973
3.46477	0.0134552	-0.0860525	0.047457
3.71236	0.0105221	-0.0678656	0.0369973
3.95995	0.0082254	-0.0534086	0.0288516
4.20754	0.00642813	-0.0419597	0.0225048
4.45512	0.00502242	-0.0329205	0.0175574
4.70271	0.00392342	-0.0258009	0.0136996
4.9503	0.00306447	-0.020204	0.0106907
5.19788	0.00239331	-0.0158107	0.00834342
5.44547	0.00186898	-0.0123663	0.00651195
5.69306	0.00145943	-0.0096683	0.00508278
5.94065	0.00113956	-0.00755652	0.00396744
6.18823	0.000889764	-0.00590452	0.00309694
6.43582	0.000694701	-0.00461278	0.00241751
6.68341	0.000542389	-0.00360308	0.00188717
6.931	0.000423462	-0.00281406	0.0014732
7.17858	0.000330607	-0.00219762	0.00115005
7.42617	0.00025811	-0.00171609	0.000897791
7.67376	0.000201508	-0.00133999	0.000700871
7.92135	0.000157318	-0.00104627	0.000547146
8.16893	0.000122818	-0.000816908	0.00042714
8.41652	9.58831e-05	-0.000637807	0.000333456
8.66411	7.48551e-05	-0.000497962	0.000260321
8.9117	5.84386e-05	-0.000388773	0.000203226
9.15928	4.56223e-05	-0.000303522	0.000158654
9.40687	3.56167e-05	-0.000236963	0.000123858
9.65446	2.78055e-05	-0.000184998	9.66932e-05
	2.17073e-05	-0.000144428	7.54864e-05
10	1.96818e-05	-0.000130952	6.84426e-05

3. Conclusion

From the image processing techniques used, much information can be extracted from satellite imagery. The vertical profiles of a satellite image can be roughly estimated. The types of aerosols present can be obtained i.e. region influenced by dust and region influenced by anthropogenic sources. The X and Y projections of the satellite imagery matrix can be obtained to investigate maximum and minimum points of satellite image. Also, the image-processing algorithm presents in clear terms to what extent some particular aerosols e.g. dust can be controlled over an area. Special regions that are not visible to the human eye can be obtained and measured in form of contours. Hence, this technique presents a more logical way of analyzing satellite imagery.

Acknowledgement

The authors appreciate the host institutions for partial sponsorship of this research.

Reference

- [1]. Emeter M.E. (2016), Numerical modelling of West Africa regional scale aerosol dispersion, Thesis submitted to Covenant University.
- [2]. Emeter M.E., Akinyemi M.L., & Akinojo O., (2015) Parametric retrieval model for estimating aerosol size distribution via the AERONET, LAGOS station, *Environmental Pollution*, 207 (C), 381-390
- [3]. ME Emeter (2017). Impacts of recirculation event on aerosol dispersion and rainfall patterns in parts of Nigeria, *GLOBAL NEST JOURNAL* 19 (2), 344-352
- [4]. Emeter, M.E., Esisio, F., Oladapo, F. (2017a). Satellite observation analysis of aerosols loading effect over Monrovia-Liberia. *Journal of Physics: Conference Series*, 852 (1), art.no. 012009, . DOI: 10.1088/1742-6596/852/1/012009
- [5]. Emeter, M.E., Onyechekwa, L., Tunji-Olayeni, P. (2017b). Effect of aerosols loading and retention on surface temperature in the DJF months. *Journal of Physics: Conference Series*, 852 (1), art. no. 012010, . DOI: 10.1088/1742-6596/852/1/012010
- [6]. Emeter, M.E., Bakeko, M., Onyechekwa, L., Ayara, W. (2017c). Altering rainfall patterns through aerosol dispersion. *Journal of Physics: Conference Series*, 852 (1), art. no. 012008, DOI: 10.1088/1742-6596/852/1/012008
- [7]. ME Emeter, ML Akinyemi, O Akin-Ojo (2016a). A novel technique for estimating aerosol optical thickness trends using meteorological parameters, *AIP Conference Proceedings* 1705 (1), 020037
- [8]. ME Emeter, ML Akinyemi, O Akinojo (2016b). Theoretical aid for improving measuring instruments efficiency within the meteorological space of Lagos-Nigeria *AIP Conference Proceedings* 1705 (1), 020054
- [9]. Yoon J., Burrows J. P., Vountas M., von Hoyningen-Huene W., Chang D. Y., Richter A., and Hilboll A., (2014). Changes in atmospheric aerosol loading retrieved from space-based measurements during the past decade, *Atmos. Chem. Phys.*, 14, 6881–6902.

- [10]. Jingfeng Huang, Chidong Zhang and Joseph M Prospero, (2009). African aerosol and large-scale precipitation variability over West Africa, *Environ. Res. Lett.* 4 015006.
- [11]. Pflug B., Main-Knorn M., Makarau A., and Richter R., (2015). Validation of aerosol estimation in atmospheric correction algorithm ATCOR, *The International Archives of the Photogrammetry, Remote Sensing and Spatial Information Sciences*, Volume XL-7/W3:677-683.
- [12]. HadjimitsisDiofantos G., (2008). Description of a New Method for Retrieving the Aerosol Optical Thickness from Satellite Remotely Sensed Imagery Using the Maximum Contrast Value and Darkest Pixel Approach, *Transaction in GIS*, 12 (5), 633–644